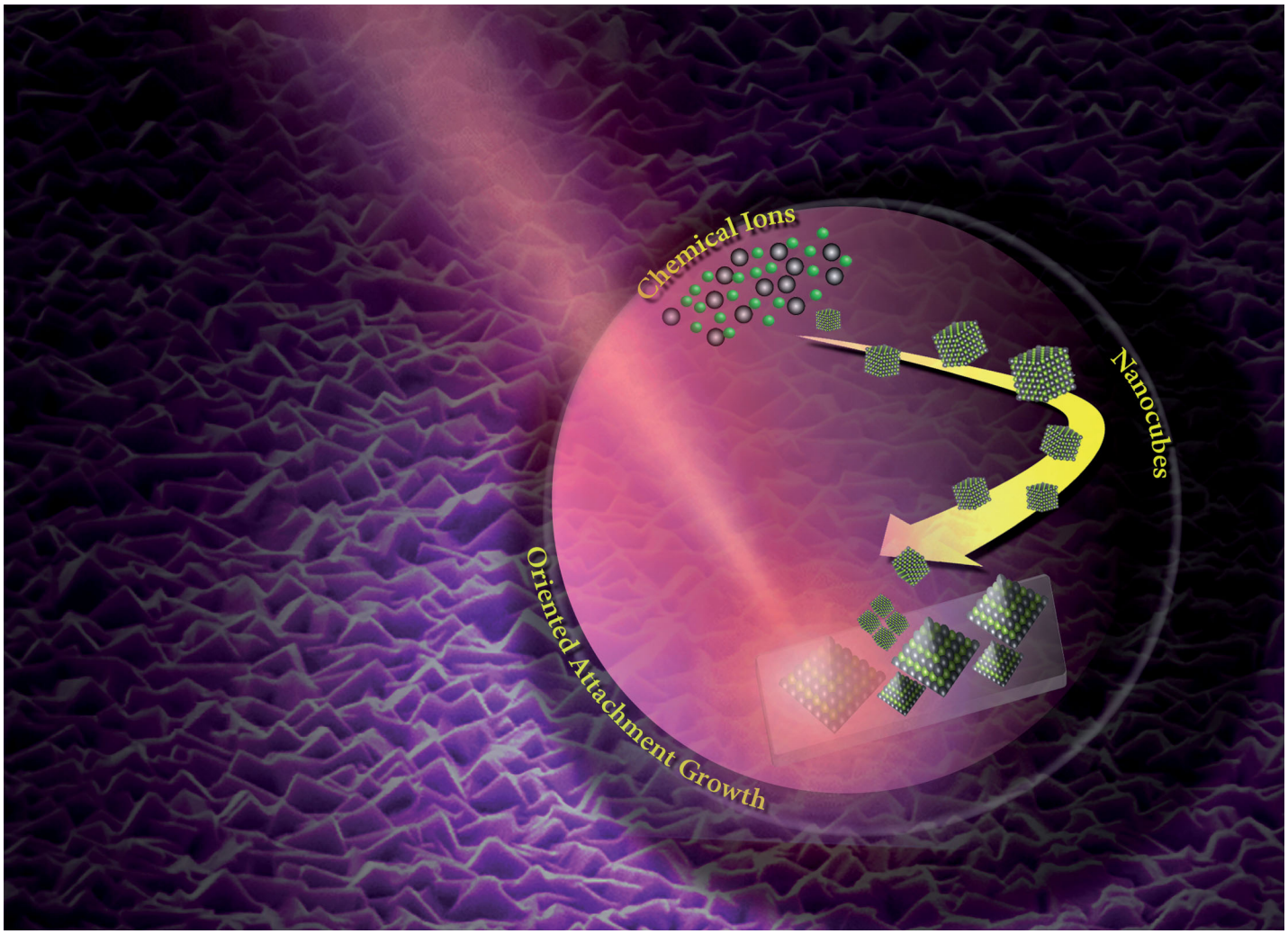

Showcasing research from the School of Electrical and Computer Engineering, University of Oklahoma, USA.

A direct oriented-attachment growth of lead-chalcogenide mid-infrared nanocrystals film on amorphous substrates

Ligand-free PbSe nanocrystals were directly assembled on amorphous glass substrates with the oriented attachment mechanism. The produced film is mirror-like and exhibits tunable quantum confinement in the MIR spectrum, which has great prospects for low-cost MIR optoelectronic applications.

As featured in:

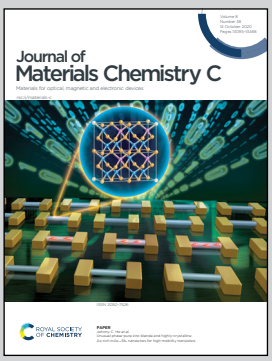

See Binbin Weng *et al.*, *J. Mater. Chem. C*, 2020, **8**, 13205.

ROYAL SOCIETY OF CHEMISTRY

rsc.li/materials-c

Registered charity number: 207890

Journal of Materials Chemistry C

ROYAL SOCIETY OF CHEMISTRY

PAPER

View Article Online
View Journal | View Issue

Cite this: J. Mater. Chem. C, 2020, 8, 13205

A direct oriented-attachment growth of lead-chalcogenide mid-infrared nanocrystals film on amorphous substrates†

Tahere Hemati, [a] Xintong Zhang [b] and Binbin Weng *[a]

Received 9th June 2020,
Accepted 23rd July 2020

DOI: 10.1039/d0tc02729d

rsc.li/materials-c

Lead-chalcogenide nanocrystals (NCs), having unique properties including the large Bohr radius, multi-exciton generation, and low Auger recombination rates, have been well received as the main choice for infrared applications. To obtain high-quality NC films on chips, hetero-compatible crystalline substrates (*e.g.*, GaAs) are commonly required. To avoid this substrate constraint, we developed a simple but non-trivial chemical deposition approach leading to a direct Oriented-Attachment (OA) growth of lead-chalcogenide NCs on amorphous substrates. Specifically, applying this new solution-based method, for the first time, (111) dominated PbSe NCs were uniformly assembled on glass slides forming mirror-like thin films of tunable quantum confining effect in the mid-infrared spectrum. Through a systematic inspection by using X-ray diffraction, electron backscatter diffraction, and photoluminescence methods, a new multi-stage OA growth model was then established to explain the dynamic chemical reaction process clearly, and thus offers a fundamentally new guideline for depositing oriented NCs on amorphous substrates directly.

1 Introduction

Lead-chalcogenide NCs have attracted a great research attention for many optoelectronic applications such as solar cells,[1,2] infrared detectors,[3,4] and light emitters.[5] The key reason stems from their unique and outstanding material properties, including the high optical conversion efficiency,[6] multi-exciton generation,[7] low Auger recombination rate,[8] and large Bohr radius[9] which results in a broad size-tunability to control bandgaps.[10]

Colloidal-based approaches like the hot-injection technique,[11–14] are commonly used to synthesize lead-chalcogenide NCs (*i.e.*, quantum dots) in solution. Their key advantage lies in the ability to control quantum dot sizes uniformly and precisely.[11] However, most colloidal methods need ligands for the NC synthesis. Unfortunately, organic ligands play the main role in preventing electronic coupling between adjacent NCs resulting in a decline in the device's electrical performance.[12,15–21] In comparison to colloidal methods, ligand-free growth methods, such as Chemical Deposition (CD) have shown a notable improvement in the electrical behavior of lead salt NCs.[22–25] Direct deposition of high-quality NC films on wafer substrates *via* the CD method has been actively explored in recent years.[26–29] It is noted that, traditionally, NC films were directly grown by the chemical deposition method, which might cause random orientation, poor crystallite uniformity, and sometimes unwanted surface contamination.[30]

In recent years, Templeman *et al.* proposed a new lead-chalcogenide CD growth model and developed a unique direct deposition method, known as the Orientate-Attachment (OA) growth, has indicated significantly enhanced uniformity and quality.[31] However, it is noticed that their direct OA growth approach can only be realized on single-crystalline GaAs substrates that require a special chemical pre-treatment before the deposition.[32] This substrate constraint substantially limits potential applications of this method in several aspects. For example, from the photonic design point of view, the high dielectric index of GaAs substrates may induce a large optical leakage from the lead-chalcogenide NC films. Besides, GaAs substrates are much costly compared to other commonly used substrates like Si or glass wafers.[33,34]

Since CD growth is a dynamic reaction process with the combination of both Ion-by-Ion (IBI) and cluster mechanisms, the NCs formation can be engineered differently depending on the chosen reaction condition. To overcome the substrate constraint and offer more freedom for synthesizing lead-chalcogenide NCs, in this work, we aim to explore a new engineering strategy based on the CD growth method to enable the direct deposition of oriented lead-chalcogenide NC films on commonly available amorphous substrates (*i.e.*, glass). It has

[a] School of Electrical and Computer Engineering, University of Oklahoma, Norman, Oklahoma 73019, USA. E-mail: binbinweng@ou.edu
[b] Center for Advanced Optoelectronic Functional Materials Research, and Key Laboratory of UV Light-Emitting Materials and Technology of Ministry of Education, Northeast Normal University, Changchun 130024, Jilin, China

† Electronic supplementary information (ESI) available. See DOI: 10.1039/d0tc02729d

been stated, Templeman *et al.*[31] have discovered the only growth zone for OA deposition of PbSe NCs on GaAs substrates. Unfortunately, none of the previous works suggests the possibility of having OA growth on amorphous glass using any single reaction condition.

Therefore, here we propose an entirely new multi-stage growth strategy, which shows a promising pathway for achieving the OA deposition on glass substrates. Considering PbSe, a lead-chalcogenide member, has critical applications in both Near-Infrared (NIR) and Mid-Infrared (MIR) field.[35–38] Herein, we carry out an extensive study of a set of control factors to grow PbSe NCs, including the complex/cations ratio, growth time, growth temperature and pH values in the solution, and develop a systematic understanding to control growth mechanism in different stages. With the new understandings, a comprehensive multi-stage growth model is developed. Hence, for the first time, the OA growth deposition of lead-chalcogenide was realized directly on the amorphous substrate successfully.

2 Experimental section

To deposit a thin layer of PbSe on the glass substrate, two precursors are needed: one for Pb cations and the other for Se anions. Moreover, to control the speed of the reaction, sodium hydroxide (NaOH) is used as a complex agent. As a Se precursor, a stock of sodium selenosulfate (Na_2SeSO_3) 0.2 M, was prepared by refluxing 0.2 M of selenium powder (Aldrich, 100 mesh, 99.99% trace metals basis) with 0.5 M of sodium sulfite (Aldrich, BioUltra, anhydrous, $\geq$98% (RT)). The Na_2SeSO_3 solution was stirred at 90 °C for 6 hours. Then, it was filtered to remove non-reacted selenium powder and was stored at 4 °C. As a Pb precursor, 0.2 M lead (II) acetate trihydrate (Aldrich, $\geq$99.99% trace metals basis) was used.

Rectangular microscope slides (3″ × 1″), were used as substrates, cleaned by solvent (acetone 55 °C, methanol 25 °C) and RCA bath (a mixture of 5 parts DI water, 1 part ammonia hydroxide and 1 part hydrogen peroxide, 70 °C/15 min). To prevent adhering large particles to the growing films, they were deposited on the bottom face of the substrates at an angle of ~70° with respect to the air–solution interface.

To prepare the deposition solution, first, the diluted lead acetate with the concentration of 48 mM was heated to reach 60 °C. Then, by adding NaOH, the pH was controlled to be in the range of 9.5–10.1. Afterward, the glass substrate is added to the Se-free solution. Finally, 48 mM of Na_2SeSO_3 was added to a 50 ml Pyrex beaker when the temperature of the final solution reached ~62 °C. Right after adding Na_2SeSO_3, the reaction solution was put away from the hot plate. It is important to mention that during the preparation, the reaction solution was continuously stirred. The reaction process will be investigated in the results and discussion section in detail.

In this research, the structural characterization of the deposited films was studied by X-ray Diffraction (XRD). The crystallographic phase and the texture of the films were studied by Rigaku Ultima IV diffractometer. Data were collected in the 2Θ geometry using Cu Kα radiation (λ = 1.5405 Å) at 40 kV and 44 mA. Diffraction scans were taken during 120 minutes over $2\Theta/\Theta$ range of 10°–70° with a step size of ~0.2°. Furthermore, the morphology of the films was observed *via* ultrahigh-resolution Ziess Neon EsB, which is a Scanning Electron Microscope (SEM). The acceleration voltage was 15 kV. Besides, Electron Backscatter Diffraction (EBSD), an SEM-based technique, provided more accurate crystallographic information, compared to the XRD about the microstructure of the sample.

Besides, the optical characterization of the deposited films was studied by reflected, and Photoluminescence (PL) emissions were measured by a Bruker Invenio-R Fourier Transform Infrared Radiation (FTIR) spectrometer in the MIR range with a 16 cm^{-1} resolution. InSb high gain detector was cooled by liquid nitrogen. To decrease the thermal background, the PL module was combined with an external SR-830 lock-in amplifier. Excitation was achieved by a 980 nm laser. Moreover, in order to study the oxidation degree in different growth mechanisms, X-ray Photoelectron Spectroscopy (XPS) was used. The XPS was performed on a system equipped with Al Kα monochromatic X-ray source. A pass energy of 20 eV was used for high-resolution scans. The total number of scans is 10, with the energy step size of 0.05 eV.

3 Results and discussion

The IBI and the cluster growth mechanisms are well-known chemical-based methods to synthesize NCs. In the IBI mechanism, the reaction between free metal ions M^{n+} (in this case Pb ions) and selenide ions Se^{2-} or, more probable HSe^-, leads to the precipitation of metal chalcogenides (PbSe) when the ionic product is greater than the solubility product.[30] In this mechanism, crystals are synthesized directly from substrate.[39] However, in the cluster growth, solid clusters precipitate in the solution and diffuse to the substrate.[31] In both mechanisms, the complex agents control the reaction rate.[40] In contrast to cluster-based nano-size crystals, IBI-based crystals typically characterized by larger grains in the micrometer regime. The reaction process, leading to the IBI, and the cluster growth, is shown in eqn (1) and (2), respectively.[30,39,41]

$$SeSO_3^{2-} + OH^- \rightarrow HSe^- + SO_4^{2-}Pb^{2+} + HSe^- + OH^- \rightarrow PbSe + H_2O \quad (1)$$

$$SeSO_3^{2-} + H_2O \rightarrow HSe^- + SeS_2O_6^{2-} + OH^-Pb(OH)_2 + HSe^- \rightarrow PbSe + OH^- + H_2O \quad (2)$$

While the IBI and the cluster mechanisms have been thoroughly investigated, only a few works were concentrated on the CD oriented-attachment growth.[31] The reported studies show the key role of the substrate in the OA growth mechanism.[42] Thus, all the given CD-based PbSe NCs by OA method, have synthesized over GaAs(111) or GaAs(100).[31,41–43] However, to the best of our knowledge, the OA-grown PbSe was realized on the glass substrate, for the first time, in this study.

Fig. 1 shows the top-view SEM images of three PbSe thin films, deposited by different growth mechanisms, on glass substrates.

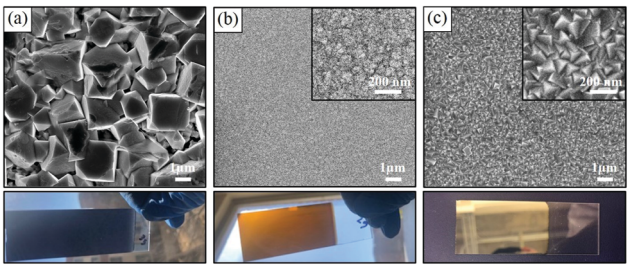

Fig. 1 Top-view SEM images of the PbSe thin film deposited by (a) a poly-crystalline high-temperature bath deposition (IBI); (b) a low-temperature quantum dots deposition (cluster); (c) the oriented-attachment growth mechanism. The appearance of the given films is shown beneath the each growth method.

Fig. 1a indicates the IBI growth, featured by large grains. The rough surface of the given film by this method, shown below the SEM image, confirms the poly-crystalline nature of this sample. Fig. 1b displays the morphology of the cluster-grown sample. The transmission of the sun-light through this sample indicates the small size of the deposited NCs. Fig. 1c shows a totally different morphology, characterized by small pyramidal-shape NCs. This film shows a shiny mirror-like look. From Fig. 1c, it seems that the pyramidal-shape NCs are mostly oriented into (111) direction. To confirm this speculation, the EBSD analysis was performed.

Fig. 2a shows the SEM image of the IBI-grown sample and Fig. 2b indicates the given Kikuchi pattern, diffracted from sample (a). Each Kikuchi line is related to the Bragg diffraction from one side of a single set of lattice planes. These lines are marked with the Miller indices, which are used to identify individual diffraction spots.[44,45] Furthermore, by scanning sample (a) on a 5 × 5 μm^2 grid, the EBSD orientation map in the form of a colored triangle is overlaid (Fig. 2c). This legend, colored Miller map provides a visual display of the spatial and angular distribution of crystallographic directions. The colored bar indicates that NCs are mostly oriented into which direction.

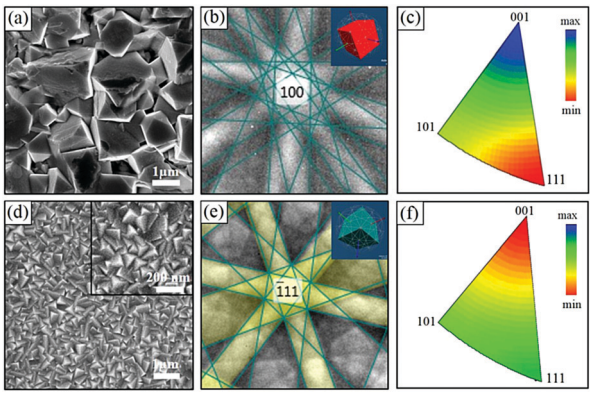

Fig. 2 (a) A top-view SEM image of the PbSe thin film deposited by IBI mechanism. (b) The Kikuchi pattern, diffracted from sample (a). (c) The EBSD orientation map of sample (a), taken on a 5 × 5 μm^2 grid. (d) A top-view SEM image of the PbSe thin film deposited by the OA mechanism. (e) The Kikuchi pattern, diffracted from sample (d). (f) The EBSD orientation map of sample (d), taken on a 5 × 5 μm^2 grid. Insets show a 3D view of (100)-oriented NCs (red cube), and (111)-oriented NCs (blue cube).

The blue region is the preferred orientation for NCs, while the red region is the least preferable. The SEM image, the Kikuchi pattern, and the EBSD orientation map of OA-grown film are shown in Fig. 2d–f, respectively.

As the given orientation map of sample (a) shows (Fig. 2c), the IBI-based NCs are mostly oriented into (001), and the [111]-oriented NCs are rare in the IBI-based sample, which considering lower surface energy of 100 facets, is not surprising. However, the orientation map of sample (d) shows an entirely different pattern. In this sample, the red zone is labeled by (001), which means, in contrast to sample (a), the (001) is the least preferable direction for NCs. Compared to sample (a), [111]-oriented NCs increased and are almost equals to [101]-oriented NCs (both shown by green zone). Therefore, according to the EBSD analysis, we suggest sample (d), indicated by pyramidal-shape NCs, is grown by a unique oriented growth mechanism, different from IBI and cluster mechanisms. In the following sections, this mechanism will thoroughly be investigated.

After the crystallographic study, optical properties of the films are then investigated here. Fig. 3a and b present the reflection spectra of both the IBI-grown and OA-grown films, respectively (incident angle = 60°). For the IBI-grown film, a clear intensity drops around 4.4 to 5 μm indicates the approximate location of the NCs' absorption-edge.[46,47] However, because the thickness of the IBI-grown film is high (*i.e.*, ~1 μm), strong interference is introduced, resulting in a broadband modulation, which raises the difficulty to precisely determine the band-gap energy from the spectrum. A simulation, thus, is performed, and a good agreement is found between the simulation and experimental results, indicating that the band-gap of the film is around 4.4 μm. The simulation detail is described in the ESI.† In terms of the thin OA-grown film with a thickness of ~300 nm, the interference can not be obviously seen in Fig. 3b. Hence, the absorption-edge can be clearly located at the wavelength close to 3 μm. To further confirm the results, PL measurements are also performed. Fig. 3c indicates the comparison of the normalized PL

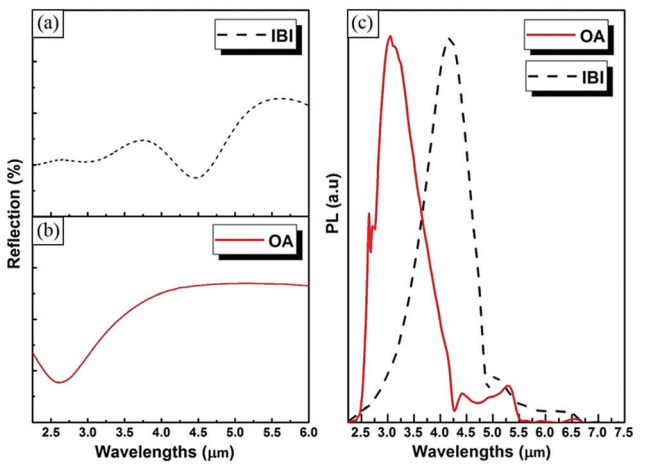

Fig. 3 (a) The reflection of the IBI-grown sample in MIR optical range. (b) The reflection of the OA-grown sample in MIR optical range. (c) The normalized PL emissions given by OA and IBI samples.

emissions given by OA and IBI deposited films. The PL peak position of the IBI sample is around 4.4 μm, which is in a good match with the given results from the sample reflection. In comparison, the peak position of the OA-grown film has blue-shifted to 3 μm. This blue-shifting indicates the reduction of the NCs' size, leading to the enhanced quantum effect.

In order to understand this newly-discovered unique OA growth mechanism, the growth rate and the related morphology changes are systematically studied. Fig. 4a shows the extracted growth rate by measuring the film thickness at different time intervals. The dramatic change in the growth rate, starting at 3rd minute, indicates the transition of the growth mechanism from the cluster to the OA. This transition is accompanied by a change in the film morphology.

Fig. 4b displays the morphology of the film deposited for three minutes. This film is characterized by the small spherical NCs, which is a typical cluster growth morphology. However, the morphology of this film is entirely different from the film deposited for 6 minutes under the same condition (Fig. 4c). Only in three minutes (growth time: 3 minutes to 6 minutes), the growth mechanism transits completely from the cluster growth to the OA mechanism. As Fig. 4a indicates, at 6th minute of growth time, there is another sharp change in the growth rate. Thus, the growth rate dramatically decreases. However, the growth rate reduction stops after 4 minutes, when the growth time is 10 minutes. Afterward, the film thickness increases with a constant rate (2.5 (nm min^{-1})). Fig. 4d shows the deposited film in 20 minutes. Apparently, the film morphology converts from the oriented pyramidal-shape to the poly-crystalline cubic-shape, which is a common morphology for the IBI mechanism.

The time-dependency of the growth rate and the related morphology changes may be attributed to the concentration of free ions in each stage of the reaction. In our study, the Pb precursor is added first, followed by adding NaOH complex, and the Se precursor is added as the final step to the hot solution (62 °C). Thus, it appears that in the initial stages of the reaction (in 3 minutes), Se^{2-} ions do not have enough time to release in the solution. Therefore, the lack of free Se^{2-} may limit the growth rate and keep the growth mechanism in the cluster regime.[30] Moreover, the formation of hydroxide clusters can be another reason that limits the free Se^{2-} ions.[31] However, in a short time, the released OH^- ions accelerate the process of Se^{2-} ions relief, which leads to a dramatic rise in the growth rate. The high temperature of the final solution facilitates sharp changes in the growth rate. As the deposition proceeds, due to the formation of PbSe, Pb^{2+} ions are removed from the solution. Thus, the complex/Pb^{2+} ratio increases, leading to the growth transition to the IBI mechanism.[30]

Generally, the free OH^- ions in the final solution have two competing roles. On the one hand, higher OH^- ions limit available free Pb^{2+} cations, on the other hand, they induce decomposition of Na_2SeSO_3 and release more Se^{2-} ions.[32] Therefore, due to the fast changes in the growth rate, resulted from OH^- ions variation, this unique OA mechanism is observed only in a narrow window, where the free OH^- ions are in the optimum amount.

As we mentioned, the consumption of free Pb^{2+} cations during the reaction leads to converting the OA growth to the IBI mechanism. Therefore, refreshing the solution to compensate the consumed free Pb^{2+} should keep the growth mechanism in the OA regime. Fig. 5 approves this explanation. Fig. 5a shows the top-view SEM imaging of the film, which was deposited for 56 minutes in total. However, every 8 minutes, the reaction solution was refreshed. The replenishing of the solution was repeated seven times. In comparison to this successive film growth, Fig. 5b indicates the morphology of the film, deposited 1 hour continuously, without replenishing the reaction solution, under the same condition. The transition growth mechanism from the OA growth to the IBI is evident. It is worth to note that the successive growth enables us to synthesize OA-deposited films up to 850 nm in thickness.

As we mentioned, during the reaction, changes in the number of free OH^- ions play a crucial role in the transition of the growth mechanism. Therefore, the amount of added NaOH, in the first place, during the preparation of the reaction solution, should have a substantial impact on the growth mechanism as well. During the preparation, we noticed that depending on the amount of added NaOH, the color of the

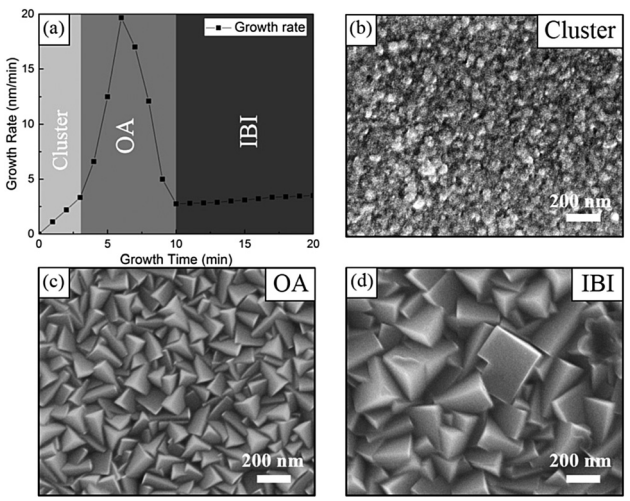

Fig. 4 (a) The plot of the growth rate as a function of growth time, labeled by three different growth mechanisms. Top-view SEM imaging of the films deposited at 45 °C, pH ~ 10, for (b) 3 minutes; (c) 6 minutes; (d) 20 minutes.

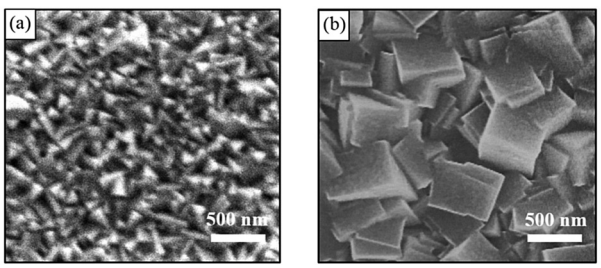

Fig. 5 A top-view SEM imaging of (a) the successively grown film deposited at 30 °C, pH 9.9, (7 runs, each run 8 minutes); (b) the deposited film at 30 °C, pH 9.9 for 60 minutes, 1 run.

solution changes. Thus, the reaction solution remains transparent when we add 0.4 M of NaOH. However, adding 0.3 M of NaOH leads to synthesizing shiny solids, which are suspended in the solution. When we decrease the amount of NaOH to 0.2 M, instead of the small suspended crystalline particles, huge agglomerated solid crystals settle down to the bottom of the reaction solution, and the solution becomes semi-transparent. The top-view SEM imaging of these three samples is shown in Fig. 6.

The SEM image of the film, deposited by the highest amount of NaOH (Fig. 6a) shows cubes randomly oriented over a layer of small connected dots. It seems that in this sample, IBI and cluster mechanisms have been initiated simultaneously. Probably, the high amount of NaOH increases the possibility of having more free OH^- ions, consequently few free Pb^{2+} cations, in the first stage of the reaction, which is in favor of IBI mechanism.[30] However, the lack of free Se^{2-} ions in the first minutes of the reaction will favor the cluster deposition.[30] Thus, it seems that the high amount of added NaOH has blocked the narrow window of realizing the OA mechanism (Fig. 4a).

However, when the amount of added NaOH is 0.3 M (Fig. 6b), the OA mechanism is completed in ten minutes. The responsible process for this mechanism has been thoroughly explained in the growth rate section (Fig. 4), where the cluster mechanism completely transited to the OA mechanism during the reaction. The observed suspended crystalline solids during the preparation may be attributed to the lead hydroxide.[30] It is noted that the color change of reaction solution slightly to the light green during the preparation stage is critically important to ensure the success of the growth. We notice that this phenomenon is caused by the uncapped operation. Thus, it is suggested that CO_2 in the air could dissolve to the solution and contribute to the growth. The involvement of CO_2 in the chemical deposition of PbSe NCs has also been observed in other studies previously.[30] We believe that CO_2 help release free OH^- ions, which promotes the synthesis of solid lead hydroxide in the Se-free solution. The XPS measurement, presented in the ESI,† reveals the effect of the uncapped operation in detail.

In the third scenario, when the amount of added NaOH decreases to 0.2 M, likely, the possibility of having more free OH^- ions, in a Se-free solution decreases. It seems that this low amount of free OH^- accelerates the relief of Pb^{2+}. Maybe this high amount of free Pb^{2+} reacts with the existing OH^- ions, results in agglomeration lead hydroxide crystals, before adding selenosulfate. In comparison to sample (b), pyramidal-shape grains of the sample (c) enlarged. This comparison suggests that decreasing added NaOH leads to enlarging the grain size. Our potential explanation for this behavior suggests that the significant amount of lead hydroxide, synthesized in the form of agglomerated crystals in the Se-free solution, may limit free Pb^{2+} cations in the final solution, which is in favor of enlarging the grain size. Thus, in a reaction solution with the lower amount of NaOH, the transition of the OA to the IBI mechanism starts in earlier stages of the reaction.

We noted during the preparation, when selenosulfate is added to the mixture of Pb acetate and NaOH, in different temperatures, the appearance of the given films looks different (ESI†). We called this temperature the preparation temperature, which is different from the growth temperature. Fig. 7a–c show the morphology of the deposited films in three different preparation temperatures. Moreover, the related PL peak position of each film is plotted in Fig. 7d.

All deposited films featured by pyramidal-shape grains, indicating the OA growth mechanism. However, comparing the SEM image of sample (a)–(c) suggests that the grain size increased slightly by increasing the preparation temperature. Furthermore, Fig. 7d shows that 10 °C raise in the preparation temperature expands NCs around 5 nm, resulting in a 300 nm red-shift in the PL peak position. The red-shift has directly resulted from the size-dependent property of the PbSe energy band-gap.[10] Moreover, by controlling the size of NCs, the PL emission was tuned over the range of [2.8–3.75 μm], the important optical range containing the molecular fingerprint of trace gases such as CO_2 and methane[48] (ESI†).

Furthermore, in order to obtain a better understanding of the OA-grown films, the XRD analysis of three films, deposited by three different growth mechanisms is performed. XRD analysis reveals more information about the structure of NCs, synthesized under different growth mechanisms. Fig. 8a and b show the SEM image and the XRD patterns of the cluster-deposited film, respectively. Fig. 8c and d display the SEM image and the XRD patterns of the IBI-deposited film, respectively.

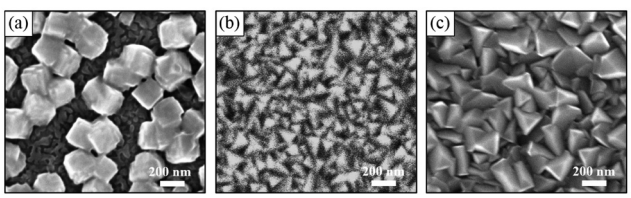

Fig. 6 A top-view SEM imaging of the film deposited at 40 °C, for 10 minutes, when (a) added NaOH = 0.4 M; (b) added NaOH = 0.3 M; (c) added NaOH = 0.2 M.

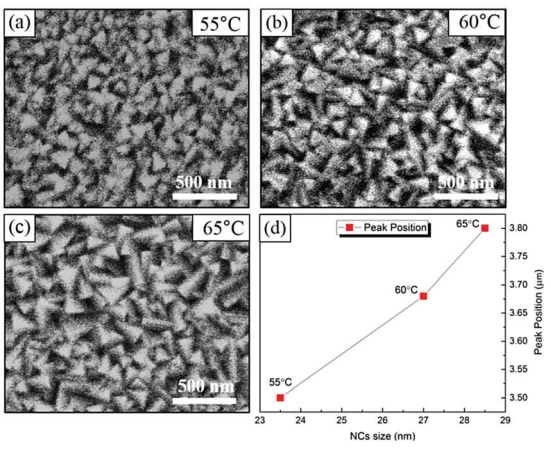

Fig. 7 A top-view SEM imaging of the film deposited at 45 °C, pH ~ 9.8, for ten minutes when the preparation temperature is (a) 55 °C, (b) 60 °C, and (c) 65 °C. (d) The plot of size-dependent PL peak position of the deposited films.

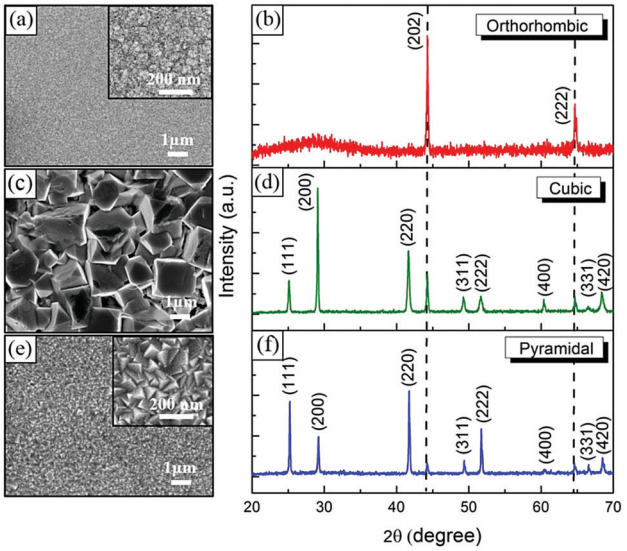

Fig. 8 (a) The SEM image of the cluster-based film. (b) X-ray diffraction patterns of sample (a). (c) The SEM image of the IBI-based film. (d) X-ray diffraction patterns of sample (c). (e) The SEM image of the OA-based film. (f) X-ray diffraction patterns of sample (e).

Besides, Fig. 8e and f indicate the SEM image and the XRD patterns of the OA-deposited film, respectively. The crystal's orientations are displayed next to each peak.

The XRD pattern of the cluster-grown sample (sample (a)), indicates two peaks at 44.1° and 64.8°, which, according to International Center Diffraction Data (ICDD), may relate to (202) and (222) facets of the orthorhombic phase of PbSe. The XRD pattern of the IBI-grown sample (sample (c)) shows ten distinct peaks. According to ICDD, we found a good match between eight peaks of the cubic phase of PbSe. These phases are depicted in Fig. 8d. However, it seems that two peaks which are displayed by the black dashed lines are not related to the cubic phase of PbSe. The position of these two peaks (black dashed line) is matched with the position of the (202) and (222) facets of the orthorhombic phase of PbSe (sample (a)). As we can see, the dominant orientation in sample (c) is (200), which is in good agreement with the given result from EBSD analysis (Fig. 2c). Finally, the XRD pattern of the OA-grown sample (sample (e)) is shown in Fig. 8f. This sample shows all peaks, appeared in sample (c); however, the peak intensity is different. *Versus* sample (c), [111]-oriented NCs are significantly increased in sample (e). However, [200]-oriented NCs are suppressed, and [220]-oriented NCs are fairly enhanced.

Existence of orthorhombic-related peaks in XRD patterns of all three samples (black dashed line), which are weak in sample (c) and (e), suggests the presence of a sub-interfacial cluster layer. The signs of the existence of this interfacial layer have already shown in Fig. 4b, where the three minutes-grown sample displays the cluster-deposited morphology. Compared to sample (c), suppressing [200]-oriented NCs and improving [111]-oriented NCs in sample (e), indicates a clear oriented growth transition. Furthermore, (111) and (220) facets of the cubic phase of PbSe may evolve from (222) and (202) facets of the orthorhombic phase of PbSe. Lastly, since XRD is performed over 5 × 5 mm^2, which is a large area, probably, the (200) peak of sample (e), originates from the contamination on the surface, which is not captured by the taken SEM image. Since the EBSD orientation map from sample (e) is scanned over a much smaller area (5 × 5 μm^2), we expect the contamination-related peak to be suppressed. Fig. 2f by showing the minimized (001) orientation would confirm this claim.

It seems that investigating each effective factor in the growth mechanism revealed a missing piece of a puzzle, which guided us toward a comprehensive understanding of the unique behavior and morphology of the OA growth. The XRD analysis, as the final piece, completed this puzzle. The XRD analysis suggested the existence of an interfacial PbSe orthorhombic seed layer, which acts as a foundation for the OA growth. Moreover, we found out the shiny particles, synthesized in the Se-free solution, are lead hydroxide crystals, which were not observed in the high-pH solutions. Furthermore, we realized the preparation temperature plays a crucial role in controlling the grain size in the OA growth mechanism. Besides, we found out the order of adding precursors possess high importance. Hence, when Se precursor is added first, no OA growth activates.

A new growth model is then proposed to offer a theoretical explanation and experimental guideline (Fig. 9). According to this model, the low pH value and the high preparation temperature lead to bonding Pb^{2+} cations to the free OH^- in the Se-free solution (Fig. 9a). The reason for emphasizing the low pH and the high preparation temperature is increasing the possibility of forming $Pb(OH)_2$. Thus, when the amount of added NaOH is too high, or similarly, the preparation temperature is not high enough (less than 45 °C), the suspended shiny particles, which we presume are $Pb(OH)_2$ were not observed,

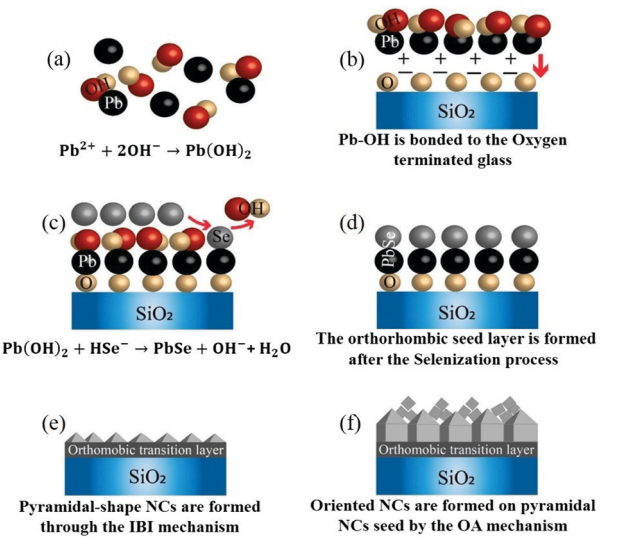

Fig. 9 Steps of the suggested growth model for the unique OA growth on the glass substrate; (a) forming lead hydroxide in the Se-free solution. (b) Bonding lead hydroxide with the oxygen terminated glass. (c) Starting Selenization process. (d) Forming a seed layer of orthorhombic PbSe NCs. (e) Synthesizing pyramidal-shape NCs on top of the seed layer by IBI growth. (f) Synthesizing OA NCs from (100) faces of pyramidal facets.

in the Se-free solution. After forming $Pb(OH)_2$, the clean glass is added to the Se-free solution. In this step, the oxygen terminated glass attracts the free lead hydroxide, in a way that the surface is terminated by hydroxide (Fig. 9b). In the third step, the Se precursor is added to the solution (Fig. 9c). Thus, through the substitution of Se^{2-} ions with hydroxide ions, the Selenization process starts in this step. In step (d), all lead hydroxide get Selenized, and an orthorhombic layer is formed. The sign of the existence of this layer is evident in the OA and the IBI mechanisms (black dashed lines in Fig. 8). We suggest that this thin film acts as a seed layer, and when the IBI growth mechanism is activated, cubic PbSe crystals tend to align with the seed layer's crystal orientation (*i.e.*, [111] and [101]). This critically important growth step is shown in Fig. 9e. On top of these oriented IBI NCs array, the later on activated OA growth mechanism will then assemble the cubic crystallites along with the bottom 100 faces (Fig. 9f). The growth mechanism is similar to the reported work by Templeman and *et al.*[31]

4 Conclusion

To conclude, OA-grown PbSe NCs were chemically synthesized directly on amorphous glass substrates, for the first time. By exploring a new domain of the pH value and the preparation temperature, a new growth zone is revealed, in which the OA growth can be realized on the amorphous glass substrate. The growth time is found to be another important factor that can control the transition of the growth mechanisms among the cluster, IBI, and OA by design. Furthermore, control factors, such as complex/cations ratio in the solution, also play a crucial role in synthesizing OA-deposited films. More importantly, a comprehensive growth model is developed through the study of these dynamic parameters, which offers a clear theoretically explanation and growth guideline of this new method. Lastly, we anticipate that this new material synthesis finding will open a new pathway to advance a wide range of optoelectronic devices such as solar cells, infrared detectors, photonic sensors, and light emitters, operating at the MIR range.

Conflicts of interest

There are no conflicts to declare.

Acknowledgements

We would like to thank Dr Preston Larson, Dr Andy Elwood Madden, and Dr Jiali Zhang for their support on material characterizations using SEM, EBSD, XRD, and AFM tools, and Dr Mark Nanny's chemical facility support.

Notes and references

1 J. N. Freitas, A. S. Gonçalves and A. F. Nogueira, *Nanoscale*, 2014, **6**, 6371–6397.
2 Y. Dou, R. Zhou, L. Wan, H. Niu, J. Zhou, J. Xu and G. Cao, *Chem. Commun.*, 2018, **54**, 12598–12601.
3 R. Saran and R. J. Curry, *Nat. Photonics*, 2016, **10**, 81.
4 Z. Ren, J. Sun, H. Li, P. Mao, Y. Wei, X. Zhong, J. Hu, S. Yang and J. Wang, *Adv. Mater.*, 2017, **29**, 1702055.
5 L. Bakueva, S. Musikhin, M. Hines, T.-W. Chang, M. Tzolov, G. D. Scholes and E. Sargent, *Appl. Phys. Lett.*, 2003, **82**, 2895–2897.
6 T. Hemati and B. Weng, *J. Appl. Phys.*, 2018, **124**, 053105.
7 R. J. Ellingson, M. C. Beard, J. C. Johnson, P. Yu, O. I. Micic, A. J. Nozik, A. Shabaev and A. L. Efros, *Nano Lett.*, 2005, **5**, 865–871.
8 P. Findlay, C. Pidgeon, R. Kotitschke, A. Hollingworth, B. Murdin, C. Langerak, A. van Der Meer, C. Ciesla, J. Oswald and A. Homer, *et al.*, *Phys. Rev. B: Condens. Matter Mater. Phys.*, 1998, **58**, 12908.
9 F. W. Wise, *Acc. Chem. Res.*, 2000, **33**, 773–780.
10 T. Hemati and B. Weng, *Nano Express*, 2020, **1**, 010030.
11 S. G. Kwon and T. Hyeon, *Small*, 2011, **7**, 2685–2702.
12 K. P. Acharya, E. Khon, T. O'Conner, I. Nemitz, A. Klinkova, R. S. Khnayzer, P. Anzenbacher and M. Zamkov, *ACS Nano*, 2011, **5**, 4953–4964.
13 C. de Mello Donegá, P. Liljeroth and D. Vanmaekelbergh, *Small*, 2005, **1**, 1152–1162.
14 H. Fu and S.-W. Tsang, *Nanoscale*, 2012, **4**, 2187–2201.
15 E. V. Ushakova, S. A. Cherevkov, A. P. Litvin, P. S. Parfenov, V. V. Zakharov, A. Dubavik, A. V. Fedorov and A. V. Baranov, *Opt. Express*, 2016, **24**, A58–A64.
16 Y. Wang, M. An, Y. Jia, L. Wang, J. Li, B. Weng, X. Zhang and Y. Liu, *Appl. Phys. Lett.*, 2019, **115**, 193902.
17 D. Zhitomirsky, O. Voznyy, S. Hoogland and E. H. Sargent, *ACS Nano*, 2013, **7**, 5282–5290.
18 Y. Gao, M. Aerts, C. S. Sandeep, E. Talgorn, T. J. Savenije, S. Kinge, L. D. Siebbeles and A. J. Houtepen, *ACS Nano*, 2012, **6**, 9606–9614.
19 S. Zhang, P. Cyr, S. McDonald, G. Konstantatos and E. Sargent, *Appl. Phys. Lett.*, 2005, **87**, 233101.
20 D. M. Balazs and M. A. Loi, *Adv. Mater.*, 2018, **30**, 1800082.
21 H. Choi, J.-G. Lee, X. D. Mai, M. C. Beard, S. S. Yoon and S. Jeong, *Sci. Rep.*, 2017, **7**, 1–8.
22 J. Qiu, B. Weng, W. Ge, L. L. McDowell, Z. Cai and Z. Shi, *Sol. Energy Mater. Sol. Cells*, 2017, **172**, 117–123.
23 I. Morales-Fernández, M. Medina-Montes, L. González, B. Gnade, M. Quevedo-López and R. Ramrez-Bon, *Thin Solid Films*, 2010, **519**, 512–516.
24 G. H. Blount, M. K. Preis, R. T. Yamada and R. H. Bube, *J. Appl. Phys.*, 1975, **46**, 3489–3499.
25 M. Ortuno-Lopez, J. Valenzuela-Jauregui, R. Ramrez-Bon, E. Prokhorov and J. González-Hernández, *J. Phys. Chem. Solids*, 2002, **63**, 665–668.
26 K. Chen, R. Kapadia, A. Harker, S. Desai, J. S. Kang, S. Chuang, M. Tosun, C. M. Sutter-Fella, M. Tsang and Y. Zeng, *et al.*, *Nat. Commun.*, 2016, **7**, 10502.
27 Q. Lin, H. J. Yun, W. Liu, H.-J. Song, N. S. Makarov, O. Isaienko, T. Nakotte, G. Chen, H. Luo and V. I. Klimov, *et al.*, *J. Am. Chem. Soc.*, 2017, **139**, 6644–6653.
28 D. Damien, A. Anil, D. Chatterjee and M. Shaijumon, *J. Mater. Chem. A*, 2017, **5**, 13364–13372.

29 Y. Wu, S. Wang and K. Komvopoulos, *J. Mater. Res.*, 2020, **35**, 76–89.
30 S. Gorer, A. Albu-Yaron and G. Hodes, *Chem. Mater.*, 1995, **7**, 1243–1256.
31 T. Templeman, S. Sengupta, N. Maman, E. Bar-Or, M. Shandalov, V. Ezersky, E. Yahel, G. Sarusi, I. Visoly-Fisher and Y. Golan, *Cryst. Growth Des.*, 2018, **18**, 1227–1235.
32 T. Templeman, M. Biton, T. Safrani, M. Shandalov, E. Yahel and Y. Golan, *CrystEngComm*, 2014, **16**, 10553–10559.
33 T. Hemati, X. Zhang and B. Weng, *Smart Photonic and Optoelectronic Integrated Circuits XXII*, 2020, p. 1128418.
34 R. A. Levy, *Novel Silicon Based Technologies*, Springer Science & Business Media, 2012, vol. 193.
35 C. S. Goldenstein, R. M. Spearrin, J. B. Jeffries and R. K. Hanson, *Prog. Energy Combust. Sci.*, 2017, **60**, 132–176.
36 T. Hemati and B. Weng, *Photonic Crystals-A Glimpse of the Current Research Trends*, IntechOpen, 2018.
37 U. Willer, M. Saraji, A. Khorsandi, P. Geiser and W. Schade, *Optics and lasers in engineering*, 2006, **44**, 699–710.
38 T.-V. Dinh, I.-Y. Choi, Y.-S. Son and J.-C. Kim, *Sens. Actuators, B*, 2016, **231**, 529–538.
39 G. Hodes, *Chemical solution deposition of semiconductor films*, CRC press, 2002.
40 S. Pawar, J. Shaikh, R. Devan, Y. Ma, D. Haranath, P. Bhosale and P. Patil, *Appl. Surf. Sci.*, 2011, **258**, 1869–1875.
41 M. Shandalov and Y. Golan, *Eur. Phys. J.: Appl. Phys.*, 2003, **24**, 13–20.
42 M. Shandalov and Y. Golan, *Eur. Phys. J.: Appl. Phys.*, 2005, **31**, 27–30.
43 M. Shandalov and Y. Golan, *Eur. Phys. J.: Appl. Phys.*, 2004, **28**, 51–57.
44 K. Saruwatari, J. Akai, Y. Fukumori, N. Ozaki, H. Nagasawa and T. Kogure, *J. Mineral. Petrol. Sci.*, 2007, **103**, 16–22.
45 W. Zhou and Z. L. Wang, *Scanning microscopy for nanotechnology: techniques and applications*, Springer science & business media, 2007.
46 P. Makuła, M. Pacia and W. Macyk, *How to correctly determine the band gap energy of modified semiconductor photocatalysts based on UV-vis spectra*, 2018.
47 J. A. Russell, *Measurement of Optical Bandgap Energies of Semiconductors*, 2011.
48 T. Hemati and B. Weng, *J. Appl. Phys.*, 2019, **125**, 154502.

